Low-Rank Decomposition and Total Variation Regularization of Hyperspectral Video Sequences

Yang Xu, *Member, IEEE*, Zebin Wu, *Senior Member, IEEE*, Jocelyn Chanussot, *Fellow, IEEE*, Mauro Dalla Mura, *Member, IEEE*, Andrea L. Bertozzi, *Member, IEEE*, and Zhihui Wei

***Abstract*— Hyperspectral video sequences (HVSs) are well suited for gas plume detection (GPD). The high spectral resolution allows the detection of chemical clouds even when they are optically thin. Processing this new type of video sequences is challenging and requires advanced image and video analysis algorithms. In this paper, we propose a novel method for GPD recorded in HVSs. Based on the assumption that the background is stationary and the gas plume is moving, the proposed method separates the background from the gas plume via a low-rank and sparse decomposition. Furthermore, taking into consideration that the gas plume is continuous in both spatial and temporal dimensions, we include total variation regularization in the constrained minimization problem, which we solve using the augmented Lagrangian multiplier method. After applying the above process to each extracted feature, a novel fusion strategy is proposed to combine the information into a final detection result. Experimental results using real data sets indicate that the proposed method achieves very promising GPD performance.**

***Index Terms*— Detection, hyperspectral video sequences (HVSs), low-rank, sparse, and total variation (LRSTV).**

Manuscript received June 30, 2017; revised September 13, 2017; accepted October 6, 2017. This work was supported in part by the National Natural Science Foundation of China under Grant 61471199, Grant 61772274, Grant 61701238, Grant 91538108, and Grant 11431015, in part by the ANR ASTRID Program under Project ANR-16-ASTR-0027-01-APHYPIS, in part by CNRS under Grant PICS-USA 263484, in part by the Jiangsu Provincial Natural Science Foundation of China under Grant BK20170858, in part by the Fundamental Research Funds for the Central Universities under Grant 30917015104, in part by the Research Fund of Jiangsu High Technology Research Key Laboratory for Wireless Sensor Networks under Grant WSNLBKF201507, and in part by the National Science Foundation under Grant DMS-1118971, NSF Grant DMS-1417674, and ONR Grant N00014-16-1-2119. *(Corresponding author: Zebin Wu.)*

Y. Xu is with the School of Computer Science and Engineering, Nanjing University of Science and Technology, Nanjing 210094, China, and also with the Grenoble Images Parole Signal Automatique Laboratory, Centre National de la Recherche Scientifique, Grenoble Institute of Technology, 38402 Grenoble, France (e-mail: xuyangth90@gmail.com).

Z. Wu is with the School of Computer Science and Engineering, Nanjing University of Science and Technology, Nanjing 210094, China, and also with the Department of Mathematics, University of California at Los Angeles, Los Angeles, CA 90095 USA (e-mail: zebin.wu@gmail.com).

J. Chanussot is with the Grenoble Images Parole Signal Automatique Laboratory, Centre National de la Recherche Scientifique, Grenoble Institute of Technology, 38402 Grenoble, France, and also with the Faculty of Electrical and Computer Engineering, University of Iceland, IS-107 Reykjavík, Iceland (e-mail: jocelyn.chanussot@gipsa-lab.fr; jocelyn@hi.is).

M. Dalla Mura is with the Grenoble Images Parole Signal Automatique Laboratory, Centre National de la Recherche Scientifique, Grenoble Institute of Technology, 38402 Grenoble, France (e-mail: mauro.dalla-mura@gipsa-lab.grenoble-inp.fr).

A. L. Bertozzi is with the Department of Mathematics, University of California at Los Angeles, Los Angeles, CA 90095 USA (e-mail: bertozzi@math.ucla.edu).

Z. Wei is with the School of Computer Science and Engineering, Nanjing University of Science and Technology, Nanjing 210094, China (e-mail: gswei@njust.edu.cn).

Color versions of one or more of the figures in this paper are available online at http://ieeexplore.ieee.org.

Digital Object Identifier 10.1109/TGRS.2017.2766094

I. Introduction

HYPERSPECTRAL imaging has been used in a number of applications such as land-use or land-cover mapping, forest inventory, or urban-area monitoring [1]–[4]. However, hyperspectral video sequences (HVSs) are much less common due to their large data size. Thanks to the dramatic improvements of sensor technologies, HVSs are currently being developed, opening the door to new research avenues and application, involving critical new methodological developments [5]–[8].

Standoff detection of chemical gas plume is necessary to environmental monitoring, emergency response, chemical warfare threat mitigation, and earth sciences [9]. However, this task still remains a challenging problem as conventional RGB images are not able to capture the potentially invisible gas plume. For example, a wide range of chemical gases have distinctive spectral signatures in the long-wave infrared (LWIR) region, requiring high resolution in the electromagnetic spectrum for detection. Another approach for plume detection utilizes temporal information by capturing multiple images. HVSs reveal the spectral properties of the scene and record its evolution over time at the cost of processing a large data hypercube [10]–[13].

Some prior work has been done on gas plume detection (GPD) in recent years. The existing works can be classified into three categories. The first category is methods based on anomaly detection. In [14]–[16], the automatic matched subspace detector (AMSD) was used to detect gas plumes and the clutter matched filter (CMF) was used to develop GPD algorithms [17], [18]. Both the AMSD and CMF detectors can detect gas plumes against a complex background, in which single-pixel false alarms are eliminated by postprocessing techniques. Thus, these methods are widely used in hyperspectral image. But in HVS, these methods can only be applied frame by frame and the postprocessing technique might be different in different scenes. The second category performs clustering of spectral data to separate the

plume from the background [8], [19], [20]. These methods often exhibit more spatial continuity. In [8], it was shown that principal component analysis (PCA) applied to each frame resulting in temporal flicker for the video, requiring a midway equalization procedure. The later works [19], [20] are able to perform graph-based clustering across several video frames, without this effect.

The third category is to extend the traditional object tracking algorithms to HVS. The mean shift tracker is applied in [12]. In [21], the position of the plume is first estimated, using the temporal redundancy between two consecutive frames. Then, a binary partition tree is built and pruned according to the previous estimation. By this way, the temporal continuity of HVS is discovered. However, the spectral characteristic of HVS is not fully used, because these methods work with only a few features of HVS.

In this paper, we propose a method to process HVS for the detection of a chemical gas plume diffusing in the atmosphere. We assume that the gas plume is the only moving object and the background of different frames is assumed to remain almost constant. Some change is allowed such as variation caused by illumination change or periodic motion of dynamic textures. Thus, it is reasonable to assume that the background information is low dimensional. Even in a static shot, there may be noise corrupting the background, but the proper low-dimensional approximation will remove this. Moreover, the gas plume is a moving object which we assume moves independently of the background. It includes spectral changes that cannot be incorporated into the low-dimensional model of background. These gas plume pixels are treated as outliers in the low-dimensional model. As the gas plume occupies only a small fraction of the image pixels, it can be treated as a sparse contribution. We assume finally that the gas plume forms a spatially and temporally connected set of pixels. Based on these assumptions, we use a low-rank and sparse matrix decomposition to separate the background from the gas plume. In addition, the total variation (TV) regularization for video can explicitly describe the gas plume continuity in both the spatial and temporal directions. In traditional moving object detection methods [22]–[27], one column of the matrix is the vectorized image of a frame; hence, only one 2-D matrix is required to represent the video. However, in HVS, there are hundreds of bands. And one 2-D matrix becomes unwieldy large in order to cover all the information contained in HVS.

To overcome this problem, we propose a novel fusion strategy called MaxD. After first performing detection in each band, it takes the maximum value of the detected gas plume part across different features. In this way, we utilize all the useful information contained in different features. The experiments on real gas plume diffusing hyperspectral videos demonstrate that our proposed model can achieve higher detection accuracies in GPD compared with the methods which only use one PC feature. Experimental results also show that the proposed method particularly performs well for target detection in noisy HVS with changing object outline. Thus, our method is well suited to GPD in HVS since the imaging quality in LWIR wavelength is lower than that in other wavelength.

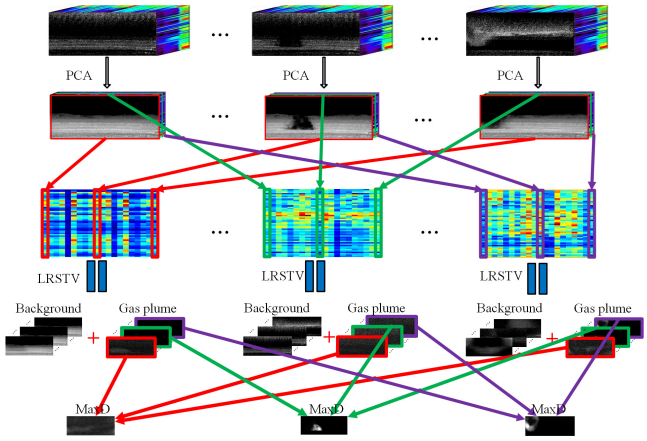

Fig. 1. Diagram showing the flowchart of the proposed detection algorithm. First, PCA is used to reduce the dimension. Then, the same PC of each frame forms a matrix that can be decomposed into the background and gas plume part by LRSTV. Finally, the detection results of different PCs are fused together using MaxD strategy.

Although the combination of the TV regularization and low-rank decomposition has been exploited in conventional video object detection [28]–[30], it is the first time to use the low-rank decomposition-based method in hyperspectral video. The advantage of hyperspectral video is the abundant spectral information that can provide us more information about the gas plume. In this paper, the TV-regularized low-rank decomposition method is used as an initial step to extract the gas plume's information from one spectral component or combination. Then, a further step is conducted which fuses the detection results of all the spectral information. In addition, both the sparse and TV constraints are imposed on the gas plume part according to the characteristic of gas plume. However, different regularization combinations are imposed on the foreground since the moving objects in [28] and [29] are different from the gas plume.

For illustrative purposes, Fig. 1 shows the flowchart of the proposed detection algorithm using a diagram. The main contributions of this paper can be therefore summarized as follows.

1) We propose a new framework of GPD in HVS different from the conventional approaches found in the literature. First, a low-rank and sparse decomposition with TV regularization is employed to produce each feature's detection result. We then use the MaxD fusion strategy to combine different features' detection results into an effective and efficient algorithm to solve the problem.
2) Taking into consideration that the gas plume is a small cluster and moves continuously between neighboring frames, we naturally incorporate the space and time connectivity by introducing TV regularization.
3) HVS contain many bands which have important spectral information. The proposed fusion strategy in the decision process allows better using the information of different features.

The rest of this paper is organized as follows. In Section II, the details of the proposed GPD method based on low-rank, sparse, and TV (GPD-LRSTV) model is described.

In Section III, experiments with real data are described and analyzed followed by conclusions in Section IV.

II. Proposed Gas Plume Detection Method

A. Problem Formulation

In the HVS, a gas plume arises in a given frame and moves during the sequence. Our goal is to separate the moving gas plume from the background. Background modeling or subtraction from video sequences is a popular approach to detect activity in a scene which finds its application in video surveillance from static cameras [27]. However, background estimation is complicated by the presence of a moving object, as well as variability in the background itself. Because background components in different frames are highly correlated, it is reasonable to assume that this variability is low rank. In addition, the foreground gas plume is spatially localized and sparse. Due to these properties, robust RPCA [31] is widely used for moving object detection. In traditional video, however, each frame is composed of one band which is vectorized as column of a matrix. Unlike these traditional videos, HVS have hundreds of bands in each frame, and it is very computational complex to put the whole frame in a column. Thus, in the first step, a one-band image is extracted at each frame. The extracted one-band image will be detailed in Section II-C. Suppose we are given an HVS including T frames, and each frame can be seen as a 3-D tensor of size $M \times N \times b$, where MM, N, and b are the number of rows, columns, and bands of each frame, respectively. Then, the vectorized one-band images are stacked as columns of a matrix $X \in \mathbb{R}^{MN \times T}$. This matrix can be expressed as the sum of a low-rank matrix modeling the background and a sparse error matrix representing the gas plume in the scene as follows:

$$\begin{aligned} &\min_{A,E} \ \operatorname{rank}(A) + \lambda \|E\|_0 \\ &\text{s.t. } A + E = X \end{aligned} \tag{1}$$

where $A \in \mathbb{R}^{MN \times T}$ represents the background matrix and $E \in \mathbb{R}^{MN \times T}$ represents the sparse error matrix. λ is a positive parameter controlling sparsity. Unfortunately, (1) is a highly nonconvex optimization problem and no efficient solution is known. A tractable optimization problem can be obtained by relaxing (1), replacing ℓ_0 norm with ℓ_1 norm and the rank norm with the nuclear norm $\|A\|_* = \sum_i \sigma_i(A)$, where $\sigma_i(A)$ is the ith singular value of A. This yields the following convex surrogate:

$$\begin{aligned} &\min_{A,E} \ \|A\|_* + \lambda \|E\|_1 \\ &\text{s.t. } A + E = X. \end{aligned} \tag{2}$$

Candès *et al.* [32] proved that the underlying low-rank matrix A and the underlying sparse matrix E can be exactly recovered with high probability.

The original work of RPCA in [31] proposed iterative thresholding methods with low complexity, but their convergence is generally very slow. Then, various algorithms have been developed for specific problems. Two of the most popular techniques are the proximal gradient (PG) method and the Augmented Lagrangian Method (ALM), both of which are applicable to a variety of convex problems. The accelerated PG (APG) methods proposed by Lin *et al.* [33] are faster and generally more accurate. The ALM [34] achieves state-of-the-art performance in terms of both speed and accuracy to the best of our knowledge. Moreover, the inexact ALM proposed in [34] requires significantly fewer partial singular value decomposition. Other methods [22]–[24] have also been proposed in the Bayesian setting. Improved models have been proposed by introducing regularizations such as adaptive graph term [35] and structured sparse term [36]. Further, nonconvex formulations of the original problem are introduced by using the Schatten-p norm [37] or a nonconvex rank approximation [38].

B. Total Variation-Regularized Low-Rank Sparse Decomposition

In our HVS, the gas plume is continuously present in the scene in both spatial and temporal dimensions. Classical object detection methods use Markov dependencies to introduce this property by adding spatial and temporal priors [23], [24]. The approximate solution to these problems can be obtained either by Markov chain Monte Carlo [39] analysis or with variational Bayesian methods [40]. In this paper, TV regularization over space–time is investigated to enforce spatial smoothness and temporal consistency. In particular, the following optimization problem is proposed:

$$\begin{aligned} &\min_{A,E} \ \|A\|_* + \lambda \|E\|_1 + \beta \|E\|_{\mathrm{TV}} \\ &\text{s.t. } A + E = X \end{aligned} \tag{3}$$

where $\|\cdot\|_{\mathrm{TV}}$ is the TV norm and β is a coefficient for the strength of that term. Before explaining the TV norm, we first define the notation that will be used.

The sparse error matrix E can be represented as a 3-D tensor $E^{\mathrm{Ten}} \in \mathbb{R}^{M \times N \times T}$, and we use $E^{\mathrm{Ten}}[m, n, t]$ to indicate the intensity of position (m, n) at frame t. To simplify the numerical computation, we stack all the entries of E^{Ten} into a column vector $E^{\mathrm{Vec}} = \mathbf{vec}(E^{\mathrm{Ten}}) \in \mathbb{R}^{MNT \times 1}$ according to the lexicographic order, where $\mathbf{vec}(\cdot)$ represents the vectorization operator.

Then, we denote $\mathbf{D}_h$, $\mathbf{D}_v$, and $\mathbf{D}_t \in \mathbb{R}^{MNT \times MNT}$ as the first-order forward finite-difference operators along the horizontal, vertical, and temporal directions, respectively. The definitions of each operator are $\mathbf{D}_h E^{\mathrm{Vec}} = \mathbf{vec}(E^{\mathrm{Ten}}[m+1, n, t] - E^{\mathrm{Ten}}[m, n, t])$, $\mathbf{D}_v E^{\mathrm{Vec}} = \mathbf{vec}(E^{\mathrm{Ten}}[m, n+1, t] - E^{\mathrm{Ten}}[m, n, t])$, and $\mathbf{D}_t E^{\mathrm{Vec}} = \mathbf{vec}(E^{\mathrm{Ten}}[m, n, t+1] - E^{\mathrm{Ten}}[m, n, t])$ with periodic boundary conditions [41].

The TV norm $\|E\|_{\mathrm{TV}}$ can either be defined as the anisotropic TV norm [42]

$$\begin{aligned} \|E\|_{\mathrm{TV}_1} = \sum_i (&\gamma_h |[\mathbf{D}_h E^{\mathrm{Vec}}]_i| \\ &+ \gamma_v |[\mathbf{D}_v E^{\mathrm{Vec}}]_i| + \gamma_t |[\mathbf{D}_t E^{\mathrm{Vec}}]_i|) \end{aligned} \tag{4}$$

or the isotropic TV norm

$$\begin{aligned} &\|E\|_{TV_2} \\ &\quad = \sum_i \sqrt{\left(\gamma_h^2 [\mathbf{D}_h E^{\mathrm{Vec}}]_i^2 + \gamma_v^2 [\mathbf{D}_v E^{\mathrm{Vec}}]_i^2 + \gamma_t^2 [\mathbf{D}_t E^{\mathrm{Vec}}]_i^2\right)} \end{aligned} \tag{5}$$

where $[\cdot]_i$ denotes the ith element of the argument and $(\gamma_h, \gamma_v, \gamma_t)$ are constants used for greater flexibility in controlling the forward difference along each direction. The anisotropic TV norm will lead to piecewise smooth solutions with defined horizontal and vertical edges in the sparse error image. The isotropic TV norm tends to produce defined and smooth edges in all directions.

Due to excellent performance suppressing discontinuous changes generally regarded as noises, TV regularization has been widely used for image and video denoising [43]–[45].

Denoting $\mathbf{D} = [\gamma_h \mathbf{D}_h^T, \gamma_v \mathbf{D}_v^T, \gamma_t \mathbf{D}_t^T]^T \in \mathbb{R}^{3MNT \times MNT}$, $\|E\|_{\mathrm{TV}_1}$ is the ℓ_1 norm of vector and $\|E\|_{TV_2}$ is the $\ell_{2,1}$ norm of vector $\mathbf{D}E^{\mathrm{Vec}}$. Thus, we can use $\|\mathbf{D}E^{\mathrm{Vec}}\|_1$ and $\|\mathbf{D}E^{\mathrm{Vec}}\|_{2,1}$ to represent $\|E\|_{\mathrm{TV}_1}$ and $\|E\|_{\mathrm{TV}_2}$, respectively.

C. Algorithm

To solve problem (3), the alternating direction method (ADM) [33] is applied. We first introduce auxiliary variable J to split the energy

$$\begin{aligned} &\min_{A,E} \ \|A\|_* + \lambda\|E\|_1 + \beta\|J\|_{\mathrm{TV}} \\ &\text{s.t } A + E = X, \quad J = E. \end{aligned} \tag{6}$$

The augmented Lagrangian function of problem (6) is

$$\begin{aligned} &L(A, E, J, Y_1, Y_2) \\ &\quad = \|A\|_* + \lambda\|E\|_1 + \beta\|J\|_{\mathrm{TV}} + \langle Y_1, X - A - E\rangle \\ &\qquad + \langle Y_2, E - J\rangle + \frac{\mu}{2}\left(\|X - A - E\|_F^2 + \|E - J\|_F^2\right) \\ &\quad = \|A\|_* + \lambda\|E\|_1 + \beta\|J\|_{\mathrm{TV}} - \frac{1}{2\mu}\left(\|Y_1\|_F^2 + \|Y_2\|_F^2\right) \\ &\qquad + \frac{\mu}{2}\left(\|X - A - E + \frac{Y_1}{\mu}\|_F^2 + \|E - J + \frac{Y_2}{\mu}\|_F^2\right) \end{aligned} \tag{7}$$

where Y_1 and Y_2 are the Lagrange multiplier matrices, μ is a positive penalty scalar, $\langle\cdot,\cdot\rangle$ denotes the matrix or Frobenius inner product, and $\|\cdot\|_F$ represents the Frobenius norm. The proposed algorithms consists in updating the variables A, E, and J repeatedly, by minimizing L with other variables fixed as well as updating dual variables Y_1 and Y_2. With some algebra, the updating schemes can be stated as follows:

$$A_{k+1} \leftarrow \arg\min_A \frac{1}{\mu}\|A\|_* + \frac{1}{2}\left\|X - A - E_k + \frac{Y_1}{\mu}\right\|_F^2 \tag{8}$$

$$\begin{aligned} E_{k+1} \leftarrow \arg\min_E \ &\frac{\lambda}{2\mu}\|E\|_1 \\ &+\frac{1}{2}\left\|E - \frac{1}{2}\left(J_k - \frac{Y_2}{\mu} + X - A_{k+1} + \frac{Y_1}{\mu}\right)\right\|_F^2 \end{aligned} \tag{9}$$

$$J_{k+1} \leftarrow \arg\min_J \frac{\beta}{\mu}\|J\|_{\mathrm{TV}} + \frac{1}{2}\left\|J - \left(E_{k+1} + \frac{Y_2}{\mu}\right)\right\|_F^2 \tag{10}$$

where (8) and (9) can be efficiently computed via the singular value thresholding (for A) and the soft thresholding operator (for E).

Then, the Lagrange multipliers are updated by $Y_1 \leftarrow Y_1 + \mu(X - A_{k+1} - E_{k+1})$ and $Y_2 \leftarrow Y_2 + \mu(E_{k+1} - J_{k+1})$.

For the sake of simplicity, subscript $k+1$ is omitted and problem (10) can be rewritten as follows:

$$J^{\mathrm{Vec}} = \arg\min_{J^{\mathrm{Vec}}} \frac{\beta}{\mu}\|\mathbf{D}J^{\mathrm{Vec}}\|_q + \frac{1}{2}\left\|J^{\mathrm{Vec}} - \mathbf{vec}\left(E + \frac{Y_2}{\mu}\right)\right\|^2 \tag{11}$$

where q represents either ℓ_1 or $\ell_{2,1}$ norm. Here, we have used the fact that the Frobenius norm of $J-(E+(Y_2/\mu))$ is the two norms of $J^{\mathrm{Vec}}-\mathbf{vec}(E+(Y_2/\mu))$, i.e., $\|J-(E+(Y_2/\mu))\|_F^2 = \|J^{\mathrm{Vec}} - \mathbf{vec}(E + (Y_2/\mu))\|^2$.

To solve the subproblem (11), another auxiliary variable $Q \in \mathbb{R}^{3MNT\times 1}$ is introduced to split this energy. Thus, we have

$$\begin{aligned} J^{\mathrm{Vec}} = \arg\min_{J^{\mathrm{Vec}}} &\frac{\beta}{\mu}\|Q\|_q + \frac{1}{2}\left\|J^{\mathrm{Vec}} - \mathbf{vec}\left(E + \frac{Y_2}{\mu}\right)\right\|^2 \\ &\text{s.t. } Q = \mathbf{D}J^{\mathrm{Vec}}. \end{aligned} \tag{12}$$

Denote $B = \mathbf{vec}(E + (Y_2/\mu))$. Then, the augmented Lagrangian function of (12) is

$$\begin{aligned} L_{J^{\mathrm{Vec}}}(J^{\mathrm{Vec}}, B, Y_3) = &\frac{\beta}{\mu}\|Q\|_q + \frac{1}{2}\|J^{\mathrm{Vec}} - B\|^2 \\ &+ Y_3^{\mathbb{T}}(Q - \mathbf{D}J^{\mathrm{Vec}}) + \frac{\eta}{2}\|Q - \mathbf{D}J^{\mathrm{Vec}}\|^2 \end{aligned} \tag{13}$$

where η is the penalty parameter associated with the quadratic penalty term $\|Q-\mathbf{D}J^{\mathrm{Vec}}\|^2$ and $Y_3 \in \mathbb{R}^{3MNT\times 1}$ is the Lagange multiplier. Again, we use the ADM to iteratively solve the problem.

Updating J^{Vec} with other terms fixed

$$\begin{aligned} J_{l+1}^{\mathrm{Vec}} \leftarrow \arg\min_{J^{\mathrm{Vec}}} &\frac{1}{2}\|J^{\mathrm{Vec}} - B\|^2 + Y_3^{\mathbb{T}}(Q_l - \mathbf{D}J^{\mathrm{Vec}}) \\ &+ \frac{\eta_l}{2}\|Q_l - \mathbf{D}J^{\mathrm{Vec}}\|^2. \end{aligned} \tag{14}$$

Setting the derivation of the objective function to zero, we have

$$(J^{\mathrm{Vec}} - B) - \mathbf{D}^{\mathbb{T}}Y_3 - \eta_l\mathbf{D}^{\mathbb{T}}(Q_l - \mathbf{D}J^{\mathrm{Vec}}) = 0. \tag{15}$$

Then, the solution of (14) is found by considering the normal equation

$$(I + \eta_l\mathbf{D}^{\mathbb{T}}\mathbf{D})J^{\mathrm{Vec}} = \mathbf{D}^{\mathbb{T}}Y_3 + \eta_l\mathbf{D}^{\mathbb{T}}Q_l + B. \tag{16}$$

Traditionally, the optimal solution can be simply obtained by computing the Moore–Penrose pseudo-inverse of $(I + \eta_l\mathbf{D}^{\mathbb{T}}\mathbf{D})$. However, this approach is computationally expensive due to the large matrix size. Due to its block-circulant structure, it can be diagonalized by the 3-D-DFT matrix [42]. Hence, (16) has the following solution:

$$\mathcal{F}^{-1}\left(\frac{\mathcal{F}(\mathbf{D}^{\mathbb{T}}Y_3 + \eta_l\mathbf{D}^{\mathbb{T}}Q_l + B)}{\mathbf{1} + \eta_l(|\mathcal{F}(\gamma_h\mathbf{D}_h)|^2 + |\mathcal{F}(\gamma_v\mathbf{D}_v)|^2 + |\mathcal{F}(\gamma_t\mathbf{D}_t)|^2)}\right) \tag{17}$$

where $\mathcal{F}(\cdot)$ denotes the 3-D Fourier transform operator, $|\cdot|^2$ is the element-wise square, and the division is element-wise. The denominator can be precalculated as it remains constant.

Updating Q_{l+1} with the other terms fixed

$$Q_{l+1} = \arg\min_{Q} \frac{\beta}{\mu}\|Q\|_q + Y_3^{\mathbb{T}}\left(Q - \mathbf{D}J_{l+1}^{\mathrm{Vec}}\right) + \frac{\eta_{l+1}}{2}\left\|Q - \mathbf{D}J_{l+1}^{\mathrm{Vec}}\right\|^2. \quad (18)$$

For $q = 1$, the solution is

$$Q_{l+1} = \mathcal{S}_{\beta/\mu\eta}\left(\mathbf{D}J_{l+1}^{\mathrm{Vec}} - Y_3/\eta_{l+1}\right) \quad (19)$$

where $\mathcal{S}(\cdot)$ is the shrinkage operator whose definition on scalars is $\mathcal{S}_\varepsilon(x) = \mathrm{sgn}(x)\max(|x| - \varepsilon, 0)$. To extend the shrinkage operator to vectors and matrix, it is applied element wise.

For $q = (2, 1)$, we first denote $Q_{l+1} = [Q_{l+1,h}^{\mathbb{T}}\ Q_{l+1,v}^{\mathbb{T}}\ Q_{l+1,t}^{\mathbb{T}}]^{\mathbb{T}}$, $Y_3 = [Y_{3,h}^{\mathbb{T}}\ Y_{3,v}^{\mathbb{T}}\ Y_{3,t}^{\mathbb{T}}]^{\mathbb{T}}$, and $W_h = \gamma_h\mathbf{D}_h J_{l+1}^{\mathrm{Vec}} - (1/\eta_{l+1})Y_{3,h}$ (analogous definitions for W_v and W_t). The solution in this case is given by

$$Q_{l+1,h} = \max(W - \beta/\mu\eta, 0)\cdot\frac{W_h}{W} \quad (20)$$

where $W = \max((|W_h|^2 + |W_v|^2 + |W_t|^2)^{1/2}, \varepsilon)$ and ε is a small constant. Here, the multiplication and division are componentwise operations.

After solving each subproblem, we update the dual variable

$$Y_3 \leftarrow Y_3 + \eta_l\left(Q_{l+1} - \mathbf{D}J_{l+1}^{\mathrm{Vec}}\right). \quad (21)$$

As mentioned in [41], the method of multipliers can achieve a faster rate of convergence by adapting the following parameter η update scheme:

$$\eta_{l+1} = \begin{cases} \rho_2\eta_l, & \text{if } \left\|Q_{l+1} - \mathbf{D}J_{l+1}^{\mathrm{Vec}}\right\| \geq \alpha\left\|Q_{l+1} - \mathbf{D}J_{l+1}^{\mathrm{Vec}}\right\| \\ \eta_l, & \text{otherwise.} \end{cases} \quad (22)$$

Here, we set $\rho_2 = 2$. After obtaining the optimal J^{Vec}, the solution of (10) is obtained by reshaping vector J^{Vec} back into the 2-D matrix variable J_{k+1}.

The complete algorithm being proposed to solve (3) is summarized in **Algorithm 1**.

Algorithm 1 Algorithm for LRSTV

Input: data matrix $\mathbf{X}$, parameters $\beta > 0$, $\lambda > 0$

Initialize 1: $A_0 = E_0 = J_0 = \mathbf{0}$, $Y_1 = X/\max(\|X\|_2, \lambda^{-1}\|X\|_\infty)$, $Y_2 = \mathbf{0}$, $\mu_0 = 1.25/\|X\|_2$, $\mu_{\max} = \mu_0 10^7$, $\rho_1 = 1.5$, $k = 0$, $\mathrm{tol}_1 = 10^{-7}$, $\mathrm{tol}_2 = 10^{-3}$.

1. **while** $|X - A_k - E_k\|_F/\|X\|_F < \mathrm{tol}_1$ **do**
2. Update variable A_{k+1}:
   $A_{k+1} = \Theta_{(1/\mu_k)}(X - E_k + (1/\mu_k)Y_1)$
   where Θ is the singular value thresholding operator [46].
3. Update variable E_{k+1}:
   $E_{k+1} = \mathcal{S}_{\lambda/(2\mu_k)}\left(\frac{J_k - (1/\mu_k)Y_2 + X - A_{k+1} + (1/\mu_k)Y_1}{2}\right)$
4. Update variable J_{k+1}:
   Solve problem:
   $\arg\min_{J^{Vec}} \frac{\beta}{\mu}\|\mathbf{D}J^{Vec}\|_q + \frac{1}{2}\|J^{Vec} - \mathbf{vec}(E_{k+1} + \frac{Y_2}{\mu})\|^2$
   Initialize 2: $J_0^{Vec} = \mathbf{vec}(E_{k+1} + \frac{Y_2}{\mu})$, $Q_0 = \mathbf{D}J_0^{Vec}$, $Y_3 = \mathbf{0}$, $l = 0$,
   compute the matrices $\mathcal{F}(\gamma_h\mathbf{D}_h)$, $\mathcal{F}(\gamma_v\mathbf{D}_v)$, $\mathcal{F}(\gamma_t\mathbf{D}_t)$,
   set $\rho_2 = 2$, $\alpha = 0.7$, $\eta_0 > 0$
   While not converged **do**
   4.1. Update J_{l+1}^{Vec} via (16)
   4.2. Update
   $Q_{l+1} = \arg\min_{Q} \frac{\beta}{\mu}\|Q\|_q + Y_3^{\mathbb{T}}(Q - \mathbf{D}J_{l+1}^{Vec}) + \frac{\eta_{l+1}}{2}\|Q - \mathbf{D}J_{l+1}^{Vec}\|^2$
   Q_{l+1} via either (18) for the anisotropic total variation or (19) for the isotropic one
   4.3. Update multiplier via (20)
   4.4. Update η_{l+1} via (21)
   4.5 Check convergence
   If $\|J_{l+1}^{Vec} - J_l^{Vec}\|_2/\|J_l^{Vec}\|_2 < \mathrm{tol}_2$ **then**
   break
   end if
   4.6. $l \leftarrow l + 1$.
   Output: optimal solution (J^{Vec}, Q)
   Reshape J^{Vec} to its 2-D matrix shape J_{k+1}
5: Update the out loop Lagrange multipliers as follows:
   $Y_1 \leftarrow Y_1 + \mu_k(X - A_{k+1} - E_{k+1})$.
   $Y_2 \leftarrow Y_2 + \mu_k(E_{k+1} - J_{k+1})$
6: Update μ as follows:
   $\mu_{k+1} = \min(\mu_{\max}, \rho_1\mu_k)$
7: $k \leftarrow k + 1$.
8: **end while**

Output: an optimal solution (A, E, J).

D. MaxD Strategy for HVS Gas Plume

In HVS, there are potentially hundreds of spectral bands. However, in the LRSTV model, only one-band video sequence is processed to separate the gas plume from the background. In order to make full use of the abundant spectral information, a preprocess step is conducted to produce the one-band video sequence before detection. The one-band video sequence should contain the sufficient information from the HVS. Band selection and feature extraction are two common technologies for preprocessing. In GPD, the corresponding bands that reveal the most information of a specific kind of gas are different, so the band selection method is applied when the gas's prior information is known. The selected band should be determined by the detected gas, but in this paper, the prior information of the detected gas is unknown; thus, band selection method cannot be treated as a common way in preprocess in regard of different gases. Besides, due to the existence of earth's surface emission, atmospheric absorbance, and sensor noise, the captured HVS has limited quality. The band selection method is not appropriate as it directly selects the one-band video sequence from the lower quality raw HVS data. To get a high-quality video sequence and design, a common method—a feature extraction method—PCA is applied in this paper. PCA is the most popular linear feature extraction method, which can keep the most information in the few components in terms of variance. Due to the low complexity and the absence of parameters, PCA is competitive for the purpose of classification and target detection of hyperspectral data [47].

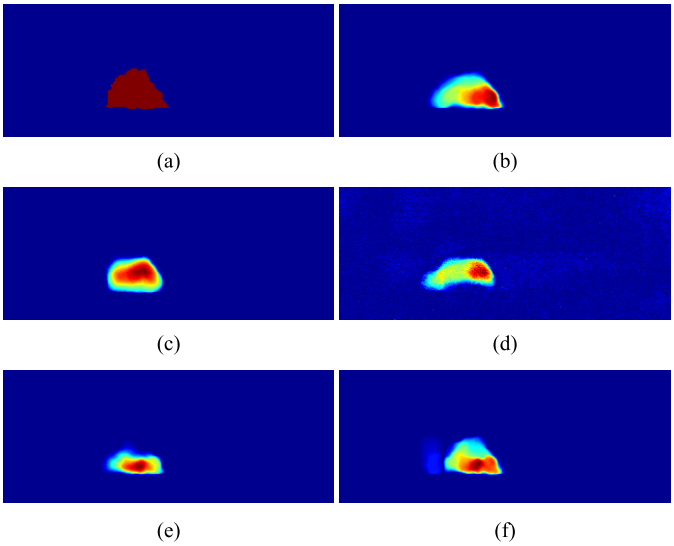

Fig. 2. HVS-aa12, frame 14. (a) Ground truth; the red pixels represents the gas plume. Then, the resulted gas plume part using (b) first, (c) second, (d) third, (e) fourth, and (f) fifth PCs. Note that for better comparison, all the gas plume images are scaled to [0, 1]. (b) and (f) are close to the ground truth, which means that the first and fifth PCs have high contrast between gas plume and background in frame 14.

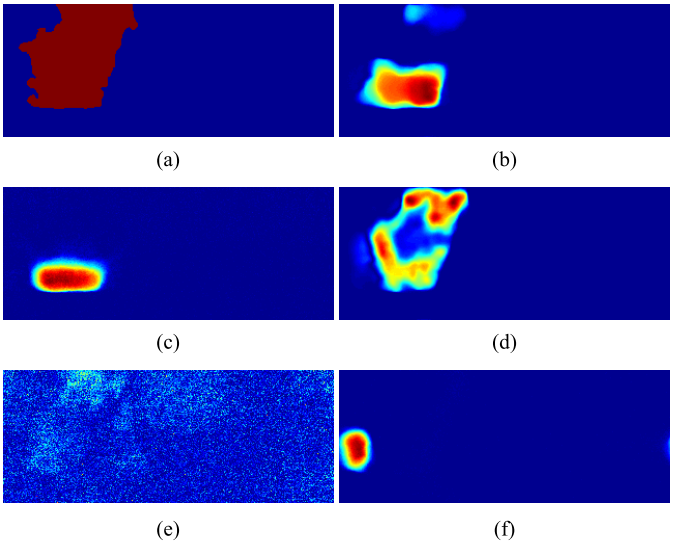

Fig. 3. HVS-aa12, frame 22. (a) Ground truth; the red pixels represent the gas plume. Then, the resulted gas plume part using (b) first, (c) second, (d) third, (e) fourth, and (f) fifth PCs. Note that for better comparison, all the gas plume images are scaled to [0, 1]. (d) is close to the ground truth, which means that the third PC has high contrast between gas plume and background in frame 22.

In this paper, for each frame of the HVS, PCA is performed and the first p components are kept. By performing PCA, the PCs act as a type of spectral filter where each component represents a particular chemical spectrum in the image. To obtain a p-dimensional representation of the data, each pixel is projected onto these p PCs. A natural strategy of GPD is to extract one feature which provides the best contrast between plume and background in each frame; then, the extracted feature can be used as the input data matrix X of Algorithm 1. However, it is hard to decide which component has the best contrast between gas plume and background. Moreover, some parts of the gas plume are obvious in one PC and some other plume parts will be obvious in other components. For example, Fig. 2(b)–(f) shows the resulted gas plume part using different PCs from frame 14, HVS-aa12. Details of HVS aa12 are presented in Section III-A. Compared to the ground-truth map [Fig. 2(a)], the first and fifth PCs have better detection results than those of the other three components. In Fig. 3(b)–(f), the gas plume part using different PCs of frame 22 HVS aa12 is shown. The third PC is the best among the first five PCs. For different frames, the best feature for detection may not be the same. Thus, it is unreasonable to use only one feature to represent the hyperpsectral image for GPD. To detect the gas plume with high probability in each frame, we propose a more robust method by combining all the features. In the first step, PCA is performed frame by frame to extract the first p PCs. Then, the ith PC of all frames are combined to form matrix X^i, where each column is each frame's ith feature. For fair comparison, all matrices X^i, $i = 1, 2, \ldots, p$ are normalized by $X^i \leftarrow (1/(\max([X^i])))X^i$, where $\max([X^i])$ represents the maximum entry of the matrix X^i. Each matrix X^i is then decomposed into the background part A^i and the plume part E^i using (3) with the same parameters λ and β. As different PCs have different projections of the original features, the resulting moving objects E^i of different PCs have different abilities to reveal the gas plume. To combine all the information, the plume detection is $\tilde{E}$ where each entry is the maximum value of all E^i at the same coordinate, which can be written as

$$\tilde{E}_{i,j} = \max\left\{E^1_{i,j}, E^2_{i,j}, \ldots, E^p_{i,j}\right\} \quad i = 1, 2, \ldots, M, \quad j = 1, 2, \ldots, N. \quad (23)$$

Here, $\tilde{E}_{i,j}$ represents the absolute value of the ith row and jth column entry of matrix $\tilde{E}$. In this way, gas plume detected by different PCs is kept. For PCs which have low contrast between background and gas plume, the corresponding moving object part E^i will be small, and it will not affect the final result as only the maximum value will be stored. Moreover, although this strategy is sensitive to noise, the TV regularization has removed the noise in prior steps. In [10], a midway method for histogram equalization is used to reduce flicker between frames. Whereas in our method, the flicker between frames will not affect the final detection because we normalize all the PCs matrix X^i and the low rank matrix is able to describe the flicker between frames. Thus, the sparse error matrix will not affect by the flicker which only shows the gas plume.

The maximum value detection strategy is noted as MaxD and the main steps for the GPD-LRSTV algorithm are shown in **Algorithm 2**.

III. Experimental Results and Discussion

In this section, we provide experimental results for our GPD algorithm with real data sets. From different perspectives, we adopt two evaluation criteria. Because the gas plume can be seen as the anomaly in each frame, we can use the receiver operating characteristic (ROC) curve to measure

Algorithm 2 Algorithm for GPD-LRSTV

Input: hyperspectral video sequence, parameters $\beta > 0$, $\lambda > 0$, p

1. Using PCA to extract the first p principal components in every frame
2. **For** $i = 1 : p$
   - 2.1. Form matrix X^i where the jth column is the vectorized ith principal component of the jth frame.
   - 2.2. Normalize X^i as follows $X^i \leftarrow \frac{1}{\max(|X^i|)} X^i$
   - 2.3. solve the following problem using **Algorithm 1**

$$\min_{A^i, E^i} \|A^i\|_* + \lambda \|E^i\|_1 + \beta \|E^i\|_{TV} \quad \text{s.t } A^i + E^i = X^i$$

End for

5. Compute the final moving object part E, subject to: $\tilde{E}_{i,j} = \max\{[E^1]_{i,j}, [E^2]_{i,j}, \ldots, [E^p]_{i,j}\}$, $i = 1, 2, \ldots, M$, $j = 1, 2, \ldots, N$

Output: an optimal solution $\tilde{E}$

the performance of the methods. A better detector would lie nearer to the top-leftmost corner and result in a larger area under the curve [48]. As more than one frame has to be compared, the area under the ROC curve (AUC) of each frame is calculated for comparison. A bigger AUC statistic represents a better performance. For quantitative evaluation, we measure the accuracy of GPD by comparing our result with the ground truth [49]. We can evaluate the results using precision and recall, which are defined as

$$\text{precision} = \frac{\text{TP}}{\text{TP} + \text{FP}}, \quad \text{recall} = \frac{\text{TP}}{\text{TP} + \text{FN}} \tag{24}$$

where TP, FP, TN, and FN are the numbers of true positives, false positives, true negatives, and false negatives, respectively. To analyze the performance, we use the F-measure

$$\text{F-measure} = 2 \cdot \frac{\text{precision} \cdot \text{recall}}{\text{precision} + \text{recall}}. \tag{25}$$

The higher the F-measure, the more accurate is the detection. In all the experiments, the final detection map is obtained by thresholding the sparse matrix. The threshold is not known in prior, and we only compare the mentioned methods. For fair comparison, we take the threshold that gives the maximal F-measure with the ground truth in all methods, thus comparing all methods' best F-measures.

The parameters $(\gamma_h, \gamma_v, \gamma_t)$ are set to (1, 1, 0.1) empirically. For λ and β, detailed discussions are presented in Section III-C. In our experiments, we adopt the isotropic TV, that is, to say $q = (2, 1)$. The number of features extracted by PCA is $p = 5$, which we find keeps most of the information in the original HVS.

A. Data Sets Description

The first two hyperspectral data sets used in our experiments were provided by the Applied Physics Laboratory at Johns Hopkins University. They consist of video sequences recorded during the release of chemical plumes at the Dugway Proving Ground. The videos were captured by three different long-wave infrared spectrometers placed at different locations to track the release of known chemicals. The cameras were about 1.25 miles away from each release at an elevation of about 1300 feet. The sensors captured one data cube every 5 s consisting of measurements at wavelengths in the LWIR portion of the electromagnetic spectrum.

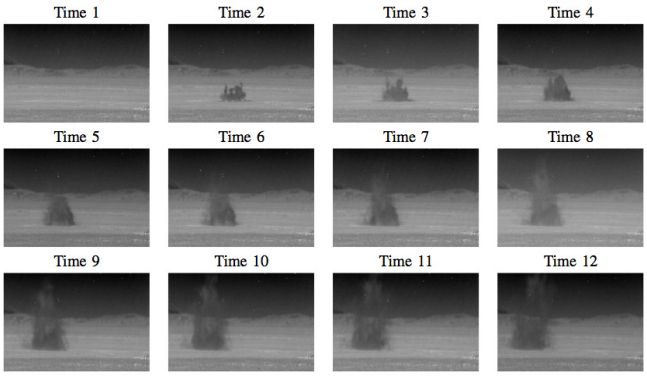

Fig. 4. First PC of 12 consecutive frames of a hyperspectral sequence.

Fig. 4 features 12 consecutive frames of a hyperspectral sequence, provided by the Applied Physics Laboratory at Johns Hopkins University.[1] They have been acquired by the US Defense Threat Reduction Agency and the National Science Foundation. Since the original data have several hundreds of spectral bands, the actual visualization of the data is not a straightforward task. For illustrative purpose, we simply plot here the first PC of each picture. This exhibits somewhat low contrast and low signal-to-noise ratio. Monitoring of the plume could be seen as a standard computer vision task of detection, segmentation, and object tracking; however, this is actually much more challenging for the following reasons.

1) The plume is not a solid object. It is impacted by significant modifications of its shape between each frame, even though there is some temporal continuity that we want to use. The tracking must take this into account.
2) The plume is not opaque. One can see the background information through it, and it has very diffuse edges. Consequently, standard segmentation is not a sufficient approach for the analysis of the data, while this should anyway be considered as a first step.
3) As previously mentioned, due to the high dimensionality of the data, many traditional image analysis methods will not work.

Furthermore, in order to evaluate the extensibility and effectiveness of our proposed detection method on traditional moving objects, we perform the experiments on a third data set, which is a sequence of 30 frame hyperspectral video

[1]The images are of dimension $128 \times 320 \times 129$, where the last dimension indicates the number of channels, each depicting a particular frequency from 7820 to 11 700 nm, spaced 30 nm apart. The sets of images were taken from videos captured by three LWIR spectrometers, each placed at a different location about 2 km away from the release of plume at an elevation of around 1300 feet. One hyperspectral image is captured every 5 s. The size of each frame is reduced to $128 \times 320 \times 5$ after PCA dimensional reduction.

TABLE I
AUC STATISTIC FOR DIFFERENT FRAMES FOR HVS-aa13

Frame Number	9	10	12	14	16	18	20	22	24	26	28	Average
GPD-IALM	0.8599	0.9886	0.9911	0.9922	0.9884	0.9441	0.8579	0.9021	0.9662	0.8724	0.6214	0.9077
GPD-DECOLOR	0.8758	0.9894	0.9932	0.9945	0.9922	0.9591	0.8896	0.9389	0.9781	0.9112	0.6748	0.9270
GPD-NRA	0.8360	0.9744	0.9885	0.9830	0.9762	0.9110	0.8569	0.8464	0.9251	0.8253	0.5562	0.8799
GPD-LRSTV	**0.9996**	**0.9997**	**0.9995**	**0.9995**	**0.9996**	**0.997**	**0.9801**	**0.9936**	**0.9969**	**0.9956**	**0.9439**	**0.9914**
GPD-LRSTV(a)	0.9811	**0.9997**	0.9994	**0.9995**	**0.9996**	0.9946	0.9765	0.9918	0.9958	0.9857	0.7654	0.9717

of a static scene with a moving box sliding from the right side of the image to the middle of the image. In each frame, 33 bands are sensed covering the range from 430 to 720 nm at 10-nm resolution, so the size of each frame is $480 \times 752 \times 33$. It is originally used to testify the restoration accuracy of a hyperspectral video of dynamic scenes from a few measured multispectral bands per frame [50].

B. Detection Results

The first data set studied is the HVS-aa13 map. It has a total of 31, with 20 containing the gas plume. Along with the HVS data, 11 frames of gas plume ground truth are provided to evaluate the performance. Qualitative and quantitative results of our methods on this data set are given.

First, to demonstrate the superiority of the introduced TV regularization, we compare our results with inexact augmented Lagrange multiplier (IALM) [34], DECOLOR [25], and nonconvex rank approximation (NRA) [38] methods. The IALM and NRA separate the background and gas plumes without considering the spatial and temporal smoothness. DECOLOR adopts the nonconvex sparsity penalty and Markov random field to detect outliers which prefers the regions that are relatively dense and contiguous. As the DECOLOR directly gives the foreground mask without tuning thresholds, it cannot be used to compute the AUC statistics and applied in the MaxD progress. We employ the difference between the original video and the background part as the detection result. Fig. 5(a) shows the 18th frame's first PC, and Fig. 5(b)–(e) shows the foreground part of the IALM, DECOLOR, NRA, and LRSTV methods, respectively. To better show the differences between these different methods, we normalize the foreground part dividing by their corresponding maximum value as shown in Fig. 5(b)–(d). The detected gas plume of LRSTV is obvious and smooth, and there is no noise in the background positions as shown in Fig. 5(d). This indicates the denoising effect of the introduced TV regularization.

Next, we use the above three methods to detect the foreground part in Algorithm 2. We denote the resulting methods using IALM, DECOLOR, NRA, and LRSTV as GPD-IALM, GPD-DECOLOR, GPD-NRA, and GPD-LRSTV, respectively. The final results are shown in Fig. 6. We see that the results are noisy except for GPD-LRSTV which is clean, similar to the ground truth. Since the gas plume dissipates, it is hard to detect by the 28th frame shown in the last row. Here, the results of GPD-IALM, GPD-DECOLOR, and GPD-NRA are rather poor. Because of the spatial and temporal continuity constraint enforced by TV regularization, our method can still recover the faded plume. GPD-LRSTV enforces continuity along the temporal dimension which penalizes rapid change between consecutive frames. To provide an objective comparison, the AUC and F-measure values of these frames are given in Tables I and II. The anisotropic TV norm is also considered for comparison. We use GPD-LRSTV(a) to denote the method using anisotropic norm. We can see that the proposed GPD-LRSTV achieves the best numerical results of every frame in terms of both AUC and F-measure statistics. GPD-LRSTV(a) achieves a similar result with GPD-LRSTV which indicates that the anisotropic TV norm and isotropic TV norm have the similar effect in the GPD.

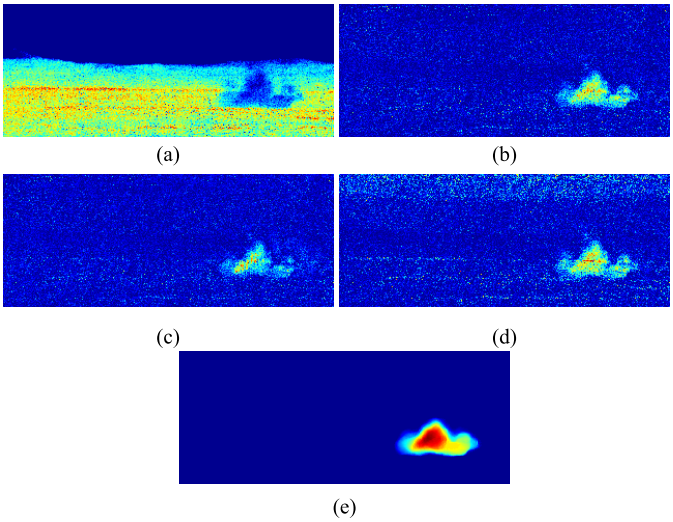

Fig. 5. (a) First PC of frame 18, HVS aa13. The detected result over the first PC using (b) IALM, (c) DECOLOR, (d) NRA, and (e) proposed LRSTV method.

The second data are the HVS-aa12 sequence. As with HVS-aa13 sequence, it has 31 frames and 20 frames with a gas plume present. The results are shown in Fig. 7. We find that GPD-IALM and GPD-NRA detect most of the gas plume, but many isolated background pixels are detected as well. The GPD-DECOLOR algorithm produces fewer incorrectly detected pixels. The GPD-LRSTV does not have this problem, and the detected gas plume is continuous. The numerical results shown in Tables III and IV prove the effectiveness of the proposed GPD-LRSTV.

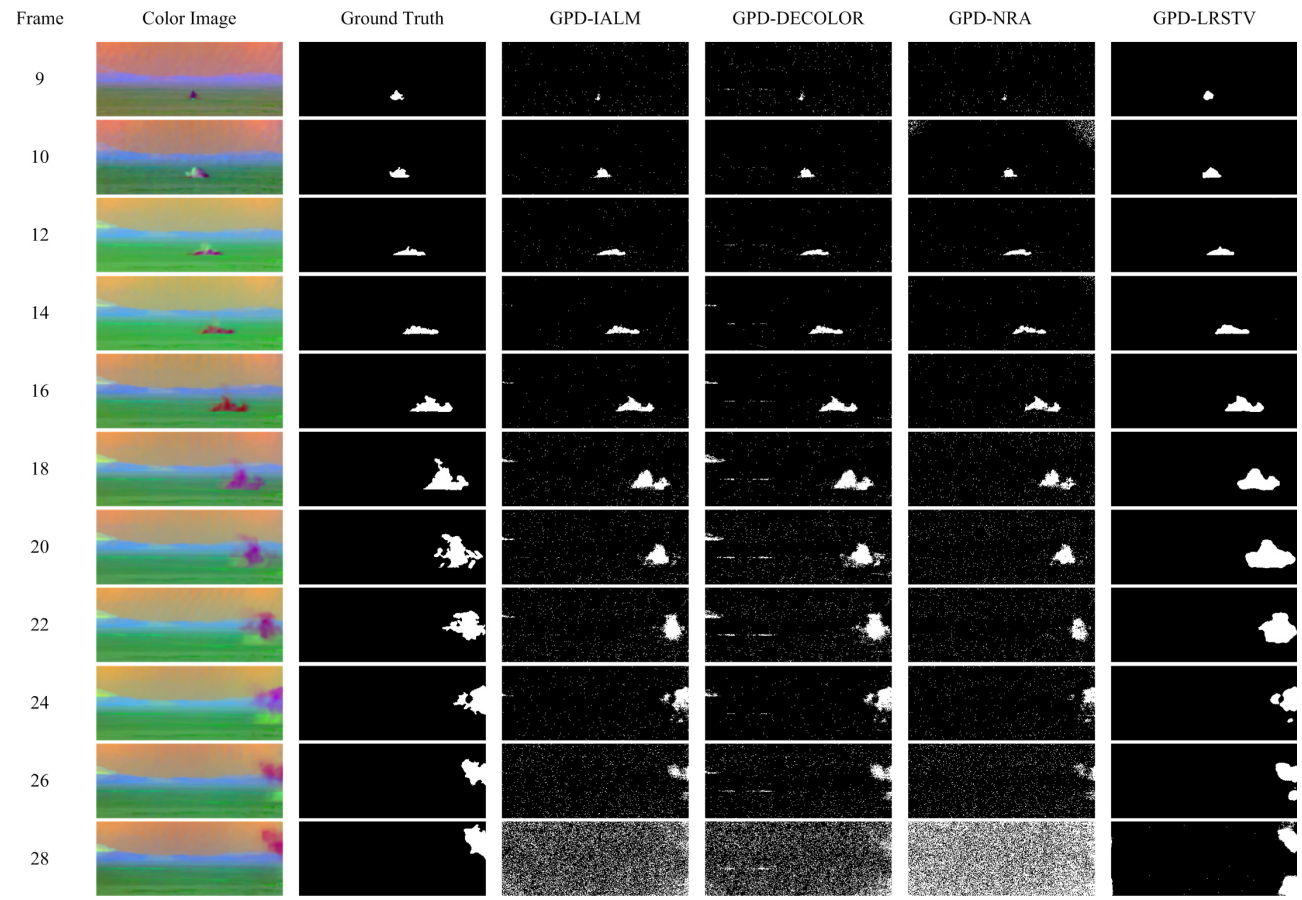

Fig. 6. Detection results of GPD-IALM, GPD-DECOLOR, GPD-NRA, and GPD-LRSTV on the HVS-aa13 sequence. First column is the false-color images of frame (9, 10, 12, 14, 16, 18, 20, 22, 24, 26, 28), respectively. Second column is the ground truth. Third and fifth columns display the results obtained by GPD-IALM and GPD-NRA, which did not consider the spatial and temporal continuity. The fourth column shows the results of GPD-DECOLOR. There still exists noise in these images calculated by GPD-DECOLOR. The sixth column is the results of GPD-LRSTV which achieves the best results especially in the last row.

TABLE II
F-MEASURE STATISTIC FOR DIFFERENT FRAMES FOR HVS-aa13

Frame Number	9	10	12	14	16	18	20	22	24	26	28	Average
GPD-IALM	0.1977	0.7251	0.7476	0.8188	0.8062	0.6789	0.4823	0.5559	0.6669	0.3462	0.0920	0.5561
GPD-DECOLOR	0.2105	0.7167	0.7222	0.7992	0.7937	0.6955	0.5198	0.6014	0.7203	0.4515	0.1157	0.5770
GPD-NRA	0.1652	0.3951	0.7234	0.7090	0.7121	0.5527	0.4250	0.4259	0.4580	0.2315	0.0751	0.4430
GPD-LRSTV	**0.8693**	0.9144	**0.9014**	**0.9107**	**0.9435**	**0.8770**	**0.7388**	**0.7962**	**0.8654**	**0.7777**	**0.5589**	**0.8321**
GPD-LRSTV(a)	0.8486	**0.9262**	0.8998	0.9209	0.9417	0.8824	0.7453	0.7860	0.8809	0.7810	0.2154	0.8026

To verify the efficiency of the proposed MaxD strategy, the detected results using a single PC are compared with the proposed GPD-LRSTV. We use the PC1-LRSTV to represent the method with $p = 1$, taking the first PC with analogous definitions for other PCs. Fig. 8(a) and (b) shows the AUC and F-measure statistics of the methods using different PCs and the full GPD-LRSTV method using five components. It can be seen that in frames 11, 12, and 14, PC1-LRSTV (LRSTV using the first PC) achieves good results, and in the following frames, PC3-LRSTV (LRSTV using the third PC) achieves good results. However, GPD-LRSTV generally achieves the best results in every frame. This demonstrates that the gas plume may not be detected by one single PC, but by taking the maximum value of the PCs' results, we can obtain a robust detection result in every frame.

Then, we apply our proposed method on the third data set. The results are shown in Fig. 9. In this video, the moving object has fixed shape and size in all frames and the differences between moving object and background is clearer than the gas plume videos. Thus, the detection task is easier in this HVS. From Fig. 9, it can be seen that all methods can detect the moving box and give a complete outline. This is because the scene is simpler and the original RPCA model can detect the moving object very well. Tables V and VI show the

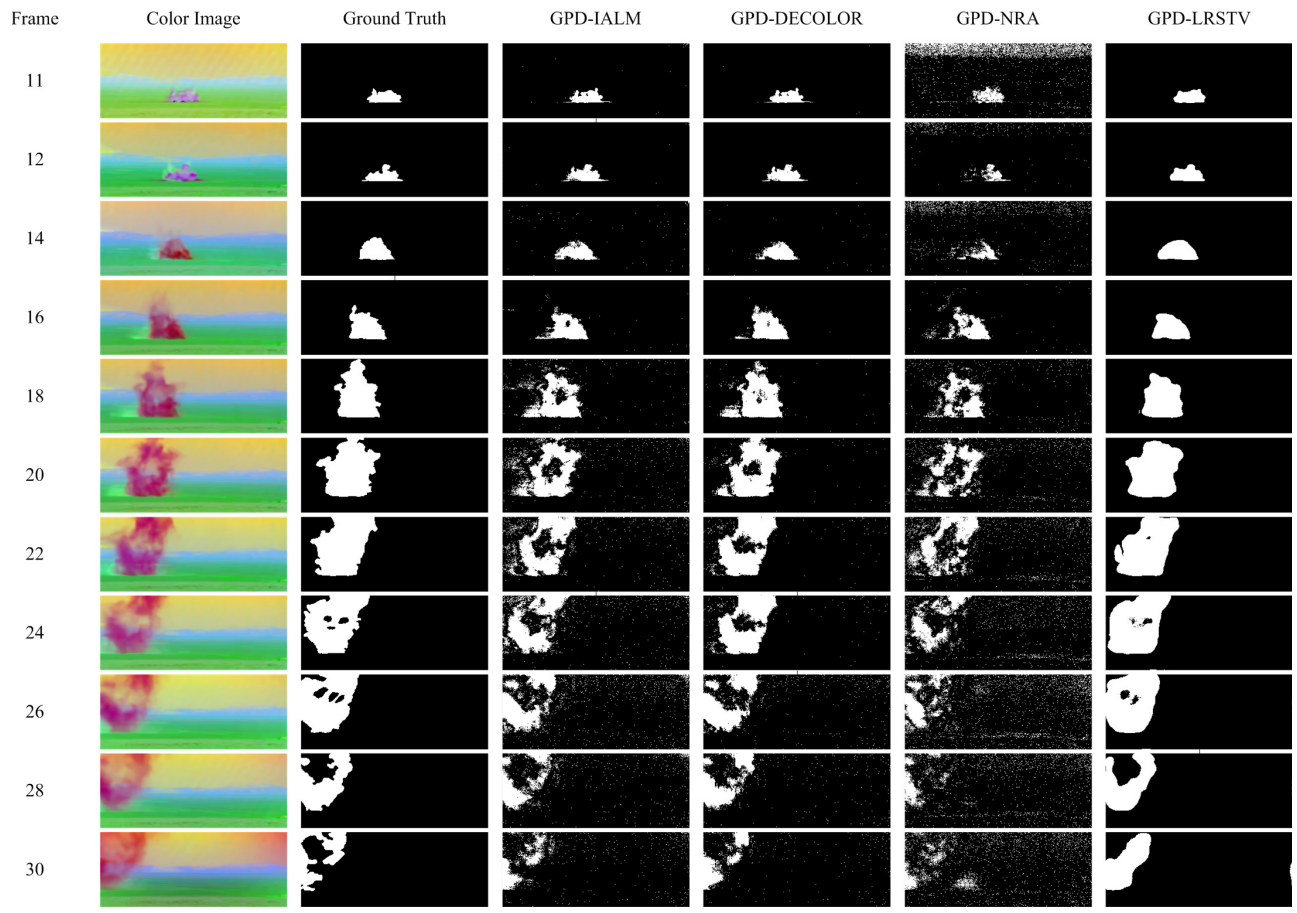

Fig. 7. Visual results of GPD-IALM, GPD-DECOLOR, GPD-NRA, and GPD-LRSTV on HVS-aa12 sequence. First column is the false-color images of frame (11, 12, 14, 16, 18, 20, 22, 24, 26, 28, 30), respectively. Second column is the ground truth. Third and fifth columns display the results obtained by GPD-IALM and GPD-NRA, which did not consider the spatial and temporal smoothness. The fourth column shows the results of GPD-DECOLOR. There also exists noise in these images calculated by GPD-DECOLOR. The sixth column is the results of GPD-LRSTV. It achieves the best results among the compared methods.

TABLE III
AUC STATISTICS FOR DIFFERENT FRAMES FOR HVS-aa12

Frame Number	11	12	14	16	18	20	22	24	26	28	30	Average
GPD-IALM	0.9898	0.9968	0.9762	0.9938	0.9192	0.8901	0.8768	0.8758	0.8536	0.9051	0.9022	0.9254
GPD-DECOLOR	0.9897	0.9973	0.9681	**0.9985**	0.9712	0.9369	0.9211	0.9125	0.8860	0.9439	0.9168	0.9493
GPD-NRA	0.8808	0.9579	0.8996	0.9616	0.8722	0.8535	0.8356	0.7782	0.7396	0.7424	0.7776	0.8454
GPD-LRSTV	**0.9984**	**0.9983**	**0.9966**	0.9984	**0.9777**	**0.9920**	**0.9901**	**0.9862**	**0.9879**	**0.9949**	**0.9281**	**0.9862**
GPD-LRSTV(a)	0.9958	0.9982	0.9936	0.9909	0.9553	0.9772	0.9768	0.9793	0.9875	0.9893	0.9067	0.9773

TABLE IV
F-MEASURE STATISTICS FOR DIFFERENT FRAMES FOR HVS-aa12

Frame Number	11	12	14	16	18	20	22	24	26	28	30	Average
GPD-IALM	0.8935	0.8830	0.8011	0.8881	0.7543	0.7291	0.7377	0.7173	0.6790	0.6975	0.6169	0.7634
GPD-DECOLOR	0.9140	**0.8860**	0.8197	**0.9401**	0.8652	0.8439	0.8483	0.8113	0.7493	0.8040	0.6911	0.8339
GPD-NRA	0.2358	0.5772	0.4093	0.7792	0.6786	0.6116	0.6211	0.5376	0.4509	0.3810	0.3511	0.5121
GPD-LRSTV	**0.9214**	0.8729	**0.8866**	0.9156	0.8823	**0.9442**	**0.9252**	**0.9065**	**0.9178**	**0.9105**	0.6612	**0.8858**
GPD-LRSTV(a)	0.9200	0.8708	0.8784	0.9226	**0.8921**	0.9247	**0.9394**	0.8982	0.9105	0.8746	**0.7059**	0.8852

AUC and F-measure statistics for HVS-MB. GPD-DECOLOR gained the best performance as DECOLOR had been proven to be effective in object detection where the object keeps the same outline and has obvious differences with the background. Besides, in HVS-MB data set, there is less noise in the scene due to the high imaging quality in 430–710-nm wavelength.

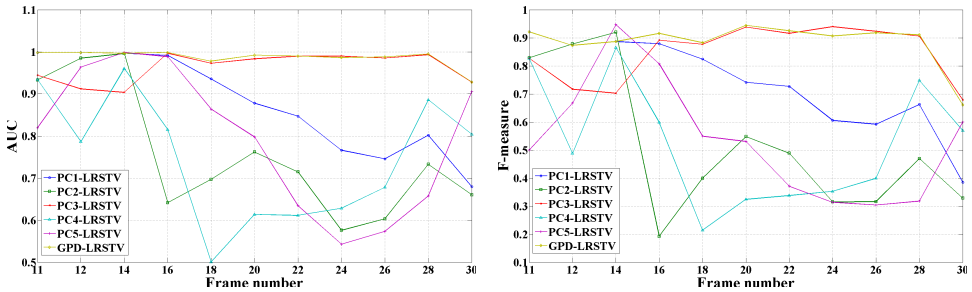

(a) (b)

Fig. 8. (a) AUC statistics for methods using different PCs and GPD-LRSTV of HVS-aa12. (b) F-measure statistics for methods using different PCs and LRSTV-MaxD of HVS-aa12. The PCn-LRSTV ($n = 1, 2, 3, 4, 5$) denotes LRSTV using the first, second, third, fourth, and fifth PCs, respectively.

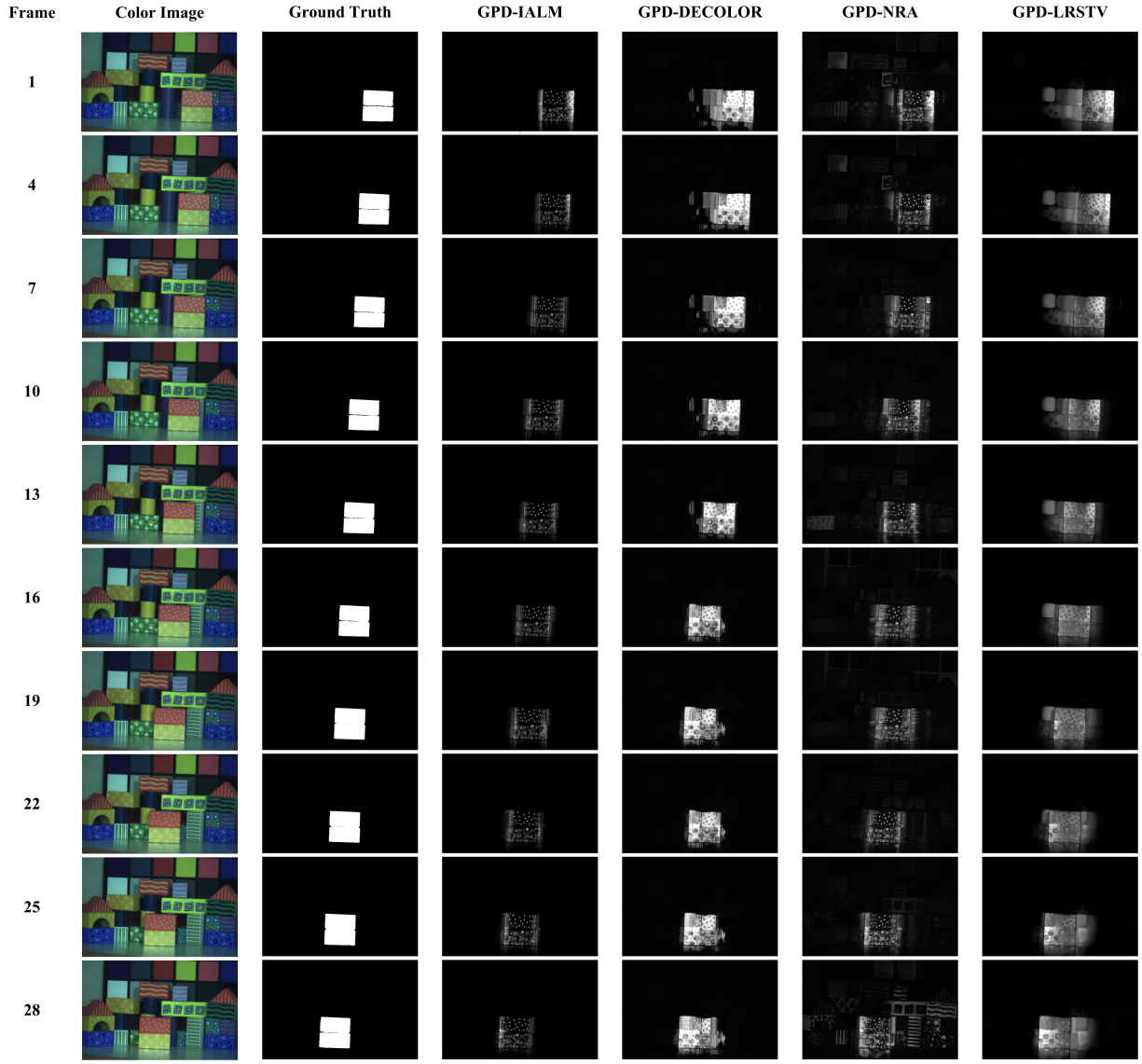

Fig. 9. Visual results of GPD-IALM, GPD-DECOLOR, GPD-NRA, and GPD-LRSTV on HVS-MB sequence. First column is the false-color images of frame (1, 4, 7, 10, 13, 16, 19, 22, 25, 28), respectively. Second column is the ground truth. Third column displays the results obtained by GPD-IALM, which did not consider the spatial and temporal smoothness. The forth column shows the results of GPD-DECOLOR. The fifth column is the results of GPD-NRA. The sixth column is the results of GPD-LRSTV.

It is reasonable that GPD-DECOLOR achieved the best results in HVS-MB. However, we can still see that the result of GPD-LRSTV is contiguous in spatial direction and has less background part being detected as moving object.

We concluded that our proposed GPD-LRSTV method achieves very competitive detection results on all the tested HVS data sets. Moreover, the TV regularization can eliminate the noise errors, thus leading to the best detection

TABLE V
AUC STATISTICS FOR DIFFERENT FRAMES FOR HVS-MB

Frame Number	1	4	7	10	13	16	19	22	25	28	Average
GPD-IALM	0.9288	0.9229	0.9092	0.9107	0.8941	0.9036	0.9083	0.8951	0.9128	0.9106	0.9096
GPD-DECOLOR	**0.9932**	**0.9941**	**0.9965**	**0.9957**	**0.9969**	**0.9968**	**0.9974**	**0.9965**	**0.9958**	**0.9929**	**0. 9956**
GPD-NRA	0.9381	0.9395	0.9572	0.9616	0.9465	0.9512	0.9413	0.9515	0.9569	0.9141	0. 9458
GPD-LRSTV	0.9816	0.9812	0.9859	0.9883	0.9916	0.9931	0.9951	0.9926	0.9858	0.9801	0.9876

TABLE VI
F-MEASURE STATISTICS FOR DIFFERENT FRAMES FOR HVS-MB

Frame Number	1	4	7	10	13	16	19	22	25	28	Average
GPD-IALM	0.6913	0.6694	0.6343	0.6301	0.6340	0.6314	0.6325	0.6359	0.6478	0.6569	0.6464
GPD-DECOLOR	**0.8096**	**0.8483**	**0.8900**	**0.8781**	**0.8981**	**0.8888**	**0.9016**	**0.9047**	**0.8783**	**0.8071**	**0.8705**
GPD-NRA	0.5057	0.5077	0.5856	0.6147	0.5209	0.5978	0.5605	0.5824	0.6205	0.4433	0.5539
GPD-LRSTV	0.6828	0.6908	0.7172	0.7602	0.8233	0.8615	0.8798	0.8444	0.7843	0.7012	0.7746

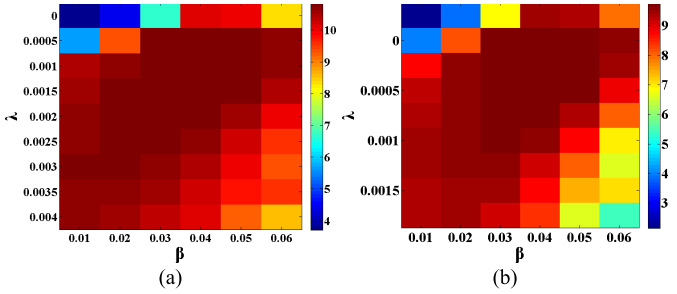

Fig. 10. Joint consideration of β and λ for HVS-aa12. (a) AUC statistics. (b) F-measure statistics.

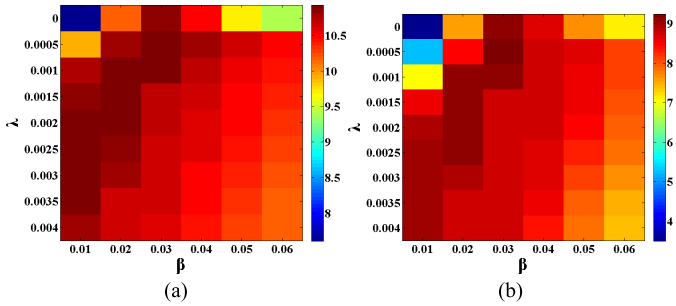

Fig. 11. Joint consideration of β and λ for HVS-aa13. (a) AUC statistics. (b) F-measure statistics.

accuracy while processing the HVS with low signal-to-noise ratio.

C. Sensitivity to the Regularization Parameters

The proposed method involves two important regularization parameters: λ and β. Ideally, we desire a robust method to select them using MAP estimation. Due to the computational complexity, we do not use a robust estimation method here. Fig. 10 illustrates the obtained AUC and F-measure of HVS-aa12 when jointly taking the two regularization parameters into consideration. To add to this, for each pair, we sum the F-measure of the 11 frames for which we have ground truth in the considered data set. λ is chosen from {0, 0.0005, 0.0001, 0.0015, 0.002, 0.0025, 0.003, 0.0035, 0.004} and β is chosen from {0.01, 0.02, 0.03, 0.04, 0.05, 0.06}. When $\beta = 0$, (3) degenerates to the RPCA problem which can be solved by IALM. The previous experiment has shown that the proposed GPD-LRSTV is superior to GPD-IALM which advocates including the advance of TV regularization. From Figs. 10 and 11, we can see that for $\lambda = 0$, the detection results are inferior to the results obtained for $\lambda > 0$. This confirms that gas plume takes a small part of the whole image scene; hence, the foreground matrix is sparse. For the aa12 sequence, GPD-LRSTV achieves a high F-measure when $\lambda \in [0.0005, 0.002]$ and $\beta \in [0.03, 0.05]$. In our experiments, we set $\lambda = 0.001$ and $\beta = 0.04$. Analogous to HVS-aa12, the best sets for HVS-aa13 are $\lambda \in [0.001, 0.002]$ and $\beta \in [0.01, 0.02]$ as shown in Fig. 10. For this HVS, we set $\lambda = 0.002$ and $\beta = 0.02$.

D. Convergence Analysis

In this section, we evaluate the convergence of LRSTV, as it is an iterative algorithm. LRSTV is applied on the first PC of HVS-aa13 data set. The residuals $\|X - A - E\|_F$ and objective function value at each iteration are computed. The curves of residual and objective function value versus the number of iterations are shown in Fig. 12, where we can clearly see that LRSTV convergences quickly.

E. Computational Complexity

The computation costs of the GPD methods have also been compared. Detailed results are presented in Table VII. The algorithms are tested on a computer with a 64-b quad-core Intel Xeon CPU 3.33-GHz processor under Windows 7. GPD-IALM, GPD-NRA, and the proposed method are implemented in MATLAB, while the core part of GPD-DECOLOR

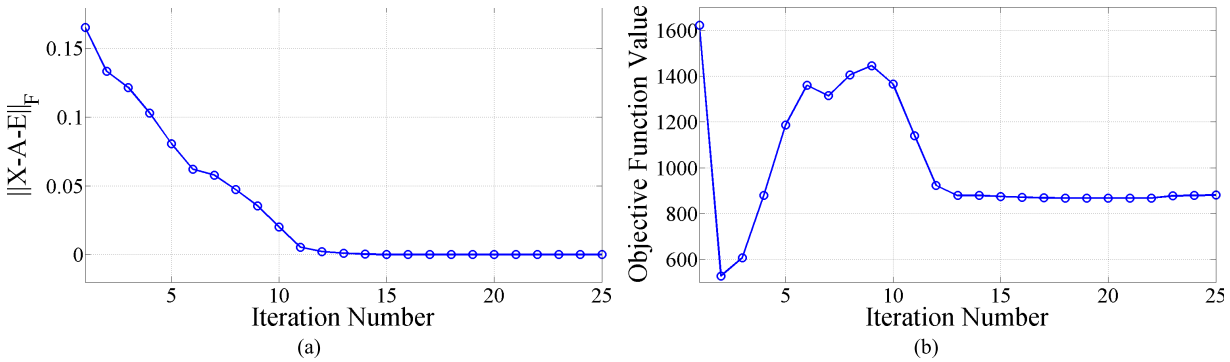

Fig. 12. Convergence analysis of LRSTV algorithm on the first PC of HVS-aa13 data set. (a) Residual over iterations. (b) Objective function value over iterations.

TABLE VII
EXECUTION TIMES (IN SECONDS) IN GPD

Data Set	GPD-IALM	GPD-DECOLOR	GPD-NRA	GPD-LRSTV
HVS-aa12	22.6573	78.8775	141.1002	824.5067
HVS-aa13	21.3319	63.0487	140.2612	827.6779

is implemented in C++. So we can infer that the methods with temporal–spatial regularization (GPD-DECOLOR, GPD-LRSTV) cost more execution time than that of original RPCA methods (GPD-IALM, GPD-NRA). In the future, we will explore parallel implementations of our proposed method on graphics processing units (GPUs) to accelerate the execution of the algorithm, which is important for the application of our proposed method.

IV. CONCLUSION AND FUTURE RESEARCH LINES

In this paper, a novel hypserspectral video sequence for GPD framework named GPD-LRSTV is proposed. It is based on the assumption that the background in different frames is reasonably stable and the moving object changes gradually in both space and time. We have formulated the variational GPD problem and introduced spatial and temporal continuity with TV regularization. Because there may exist hundreds of bands in an HVS, it is hard to extract a single band or feature to use for the LRSTV model. Thus, we adopt a novel strategy which takes the maximum value over each PC's detection result. This way, we obtain a robust detection for every frame. Our results on three HVSs demonstrate the advantage of GPD-LRSTV.

The proposed method works well when the background is static. The case of dynamic background is for the future work. Another important aspect deserving future research is the computational complexity of the proposed method. In this regard, we are currently developing efficient implementations using high-performance computing architectures such as commodity GPUs.

REFERENCES

[1] P. Ghamisi, J. A. Benediktsson, and M. O. Ulfarsson, "Spectral–spatial classification of hyperspectral images based on hidden Markov random fields," *IEEE Trans. Geosci. Remote Sens.*, vol. 52, no. 5, pp. 2565–2574, May 2014.

[2] L. Sun, Z. Wu, J. Liu, L. Xiao, and Z. Wei, "Supervised spectral–spatial hyperspectral image classification with weighted Markov random fields," *IEEE Trans. Geosci. Remote Sens.*, vol. 53, no. 3, pp. 1490–1503, Mar. 2015.

[3] Y. Xu, Z. Wu, J. Li, A. Plaza, and Z. Wei, "Anomaly detection in hyperspectral images based on low-rank and sparse representation," *IEEE Trans. Geosci. Remote Sens.*, vol. 54, no. 4, pp. 1990–2000, Apr. 2016.

[4] N. Yokoya, T. Yairi, and A. Iwasaki, "Coupled nonnegative matrix factorization unmixing for hyperspectral and multispectral data fusion," *IEEE Trans. Geosci. Remote Sens.*, vol. 50, no. 2, pp. 528–537, Feb. 2012.

[5] Y. Xu, Z. Wu, Z. Wei, M. D. Mura, J. Chanussot, and A. L. Bertozzi, "GAS plume detection in hyperspectral video sequence using low rank representation," in *Proc. IEEE Int. Conf. Image Process. (ICIP)*, Sep. 2016, pp. 2221–2225.

[6] S. Henrot, J. Chanussot, and C. Jutten, "Dynamical spectral unmixing of multitemporal hyperspectral images," *IEEE Trans. Image Process.*, vol. 25, no. 7, pp. 3219–3232, Jul. 2016.

[7] P.-A. Thouvenin, N. Dobigeon, and J.-Y. Tourneret, "Online unmixing of multitemporal hyperspectral images accounting for spectral variability," *IEEE Trans. Image Process.*, vol. 25, no. 9, pp. 3979–3990, Sep. 2016.

[8] E. Murkerjev, J. Sunu, and A. L. Bertozzi, "Graph MBO method for multiclass segmentation of hyperspectral stand-off detection video," in *Proc. IEEE Int. Conf. Image Process. (ICIP)*, Oct. 2014, pp. 689–693.

[9] D. G. Manolakis, S. Golowich, and R. DiPietro, "Long-wave infrared hyperspectral remote sensing of chemical clouds: A focus on signal processing approaches," *IEEE Signal Process. Mag.*, vol. 31, no. 4, pp. 120–141, Jul. 2014.

[10] T. Gerhart *et al.*, "Detection and tracking of gas plumes in LWIR hyperspectral video sequence data," *Proc. SPIE*, vol. 8743, p. 87430J, May 2013.

[11] A. Banerjee, P. Burlina, and J. Broadwater, "Hyperspectral video for illumination-invariant tracking," in *Proc. 1st Workshop Hyperspectral Image Signal Process., Evol. Remote Sens. (WHISPERS)*, Aug. 2009, pp. 1–4.

[12] H. Van Nguyen, A. Banerjee, and R. Chellappa, "Tracking via object reflectance using a hyperspectral video camera," in *Proc. IEEE Comput. Soc. Conf. Comput. Vis. Pattern Recognit. Workshops (CVPRW)*, Jun. 2010, pp. 44–51.

[13] C. S. Grant, T. K. Moon, J. H. Gunther, M. R. Stites, and G. P. Williams, "Detection of amorphously shaped objects using spatial information detection enhancement (SIDE)," *IEEE J. Sel. Topics Appl. Earth Observ. Remote Sens.*, vol. 5, no. 2, pp. 478–487, Apr. 2012.

[14] J. B. Broadwater, D. Limsui, and A. K. Carr, "A primer for chemical plume detection using LWIR sensors," Johns Hopkins Univ. Applied Phys. Lab, Laurel, MD, USA, Tech. Rep. NSTD-11-0661, Apr. 2011.

[15] J. B. Broadwater, T. S. Spisz, and A. K. Carr, "Detection of gas plumes in cluttered environments using long-wave infrared hyperspectral sensors," *Proc. SPIE*, vol. 6954, p. 69540R, Apr. 2008.

[16] E. M. O'Donnell, D. W. Messinger, C. Salvaggio, and J. R. Schott, "Identification and detection of gaseous effluents from hyperspectral imagery using invariant algorithms," *Proc. SPIE*, vol. 5425, pp. 573–582, Aug. 2004.

[17] V. Farley, A. Vallières, A. Villemaire, M. Chamberland, P. Lagueux, and J. Giroux, "Chemical agent detection and identification with a hyperspectral imaging infrared sensor," *Proc. SPIE*, vol. 6739, p. 673918, Nov. 2007.

[18] A. Vallières *et al.*, "Algorithms for chemical detection, identification and quantification for thermal hyperspectral imagers," *Proc. SPIE*, vol. 5995, p. 59950G, Nov. 2005.

[19] E. Hirsch and E. Agassi, "Detection of gaseous plumes in IR hyperspectral images using hierarchical clustering," *Appl. Opt.*, vol. 46, no. 25, pp. 6368–6374, 2007.

[20] H. Hu, J. Sunu, and A. L. Bertozzi, "Multi-class graph mumford-shah model for plume detection using the MBO scheme," in *Proc. EMMCVPR*, 2015, pp. 209–222.

[21] G. Tochon, J. Chanussot, J. Gilles, M. D. Mura, J.-M. Chang, and A. L. Bertozzi, "Gas plume detection and tracking in hyperspectral video sequences using Binary Partition Trees," in *Proc. IEEE Workshop Hyperspectral Image Signal Process., Evol. Remote Sensing (WHISPERS)*, Jun. 2014, pp. 1–4.

[22] S. D. Babacan, M. Luessi, R. Molina, and A. K. Katsaggelos, "Sparse Bayesian methods for low-rank matrix estimation," *IEEE Trans. Signal Process.*, vol. 60, no. 8, pp. 3964–3977, Aug. 2012.

[23] X. Ding, L. He, and L. Carin, "Bayesian robust principal component analysis," *IEEE Trans. Image Process.*, vol. 20, no. 12, pp. 3419–3430, May 2011.

[24] N. Wang and D.-Y. Yeung, "Bayesian robust matrix factorization for image and video processing," in *Proc. IEEE Int. Conf. Comput. Vis. (ICCV)*, Jun. 2013, pp. 1785–1792.

[25] X. Zhou, C. Yang, and W. Yu, "Moving object detection by detecting contiguous outliers in the low-rank representation," *IEEE Trans. Pattern Anal. Mach. Intell.*, vol. 35, no. 3, pp. 597–610, Mar. 2013.

[26] C. Dang and H. Radha, "RPCA-KFE: Key frame extraction for video using robust principal component analysis," *IEEE Trans. Image Process.*, vol. 24, no. 11, pp. 3742–3753, Nov. 2015.

[27] C. Liu, P. C. Yuen, and G. Qiu, "Object motion detection using information theoretic spatio-temporal saliency," *Pattern Recognit.*, vol. 42, no. 11, pp. 2897–2906, 2009.

[28] W. Cao *et al.*, "Total variation regularized tensor RPCA for background subtraction from compressive measurements," *IEEE Trans. Image Process.*, vol. 25, no. 9, pp. 4075–4090, Sep. 2016.

[29] X. Cao, L. Yang, and X. Guo, "Total variation regularized RPCA for irregularly moving object detection under dynamic background," *IEEE Trans. Cybern.*, vol. 46, no. 4, pp. 1014–1027, Apr. 2016.

[30] R. Chartrand, "Nonconvex splitting for regularized low-rank+ sparse decomposition," *IEEE Trans. Signal Process.*, vol. 60, no. 11, pp. 5810–5819, Nov. 2012.

[31] J. Wright, A. Ganesh, S. Rao, Y. Peng, and Y. Ma, "Robust principal component analysis: Exact recovery of corrupted low-rank matrices via convex optimization," in *Proc. Adv. Neural Inf. Process. Syst. (NIPS)*, 2009, pp. 2080–2088.

[32] E. J. Candès, X. Li, Y. Ma, and J. Wright, "Robust principal component analysis?" *J. ACM*, vol. 58, no. 1, pp. 1–37, 2009.

[33] Z. Lin, A. Ganesh, and J. Wright, "Fast convex optimization algorithms for exact recovery of a corrupted low-rank matrix," in *Proc. Comput. Adv. Multi-Sensor Adapt. Process. (CAMSAP)*, 2009, pp. 1–18.

[34] M. Chen, Z. Lin, L. Wu, and Y. Ma, "The augmented Lagrange multiplier method for exact recovery of corrupted low-rank matrices," Coordinated Sci. Lab., Urbana, IL, USA, Tech. Rep. DC-247 (UILU-ENG 09-2215), 2009.

[35] G.-F. Lu, Y. Wang, and J. Zou, "Low-rank matrix factorization with adaptive graph regularizer," *IEEE Trans. Image Process.*, vol. 25, no. 5, pp. 2196–2205, May 2016.

[36] X. Liu, G. Zhao, J. Yao, and C. Qi, "Background subtraction based on low-rank and structured sparse decomposition," *IEEE Trans. Image Process.*, vol. 24, no. 8, pp. 2502–2514, Aug. 2015.

[37] J. Wang, M. Wang, X. Hu, and S. Yan, "Visual data denoising with a unified Schatten-p norm and ℓq norm regularized principal component pursuit," *Pattern Recognit.*, vol. 48, no. 10, pp. 3135–3144, 2015.

[38] Z. Kang, C. Peng, and Q. Cheng, "Robust PCA via nonconvex rank approximation," in *Proc. IEEE Int. Conf. Data Mining (ICDM)*, Nov. 2015, pp. 211–220.

[39] C. P. Robert and G. Casella, *Monte Carlo Statistical Methods*, 2nd ed. New York, NY, USA: Springer, 2004.

[40] M. J. Beal, "Variational algorithms for approximate Bayesian inference," Ph.D. dissertation, Gatsby Comput. Neurosci. Unit, Univ. College London, London, U.K., 2003.

[41] B. Kim, "Numerical optimization methods for image restoration," Ph.D. dissertation, Dept. Manage. Sci. Eng., Stanford Univ., Stanford, CA, USA Dec. 2002.

[42] S. H. Chan, R. Khoshabeh, K. B. Gibson, P. E. Gill, and T. Q. Nguyen, "An augmented Lagrangian method for total variation video restoration," *IEEE Trans. Image Process.*, vol. 20, no. 11, pp. 3097–3111, Nov. 2011.

[43] W. He, H. Zhang, L. Zhang, and H. Shen, "Total-variation-regularized low-rank matrix factorization for hyperspectral image restoration," *IEEE Trans. Geosci. Remote Sens.*, vol. 54, no. 1, pp. 178–188, Jan. 2016.

[44] W. Zhu *et al.*, "Unsupervised classification in hyperspectral imagery with nonlocal total variation and primal-dual hybrid gradient algorithm," *IEEE Trans. Geosci. Remote Sens.*, vol. 55, no. 5, pp. 2786–2798, May 2017.

[45] Q. Cheng, H. Shen, L. Zhang, and P. Li, "Inpainting for remotely sensed images with a multichannel nonlocal total variation model," *IEEE Trans. Geosci. Remote Sens.*, vol. 52, no. 1, pp. 175–187, Jan. 2014.

[46] J. F. Cai, E. J. Candès, and Z. Shen, "A singular value thresholding algorithm for matrix completion," *SIAM J. Optim.*, vol. 20, no. 4, pp. 1956–1982, 2010.

[47] J. A. Richards and X. Jia, *Remote Sensing Digital Image Analysis: An Introduction*. New York, NY, USA: Springer-Verlag, 2006.

[48] D. Manolakis and G. S. Shaw, "Detection algorithms for hyperspectral imaging applications," *IEEE Signal Process. Mag.*, vol. 19, no. 1, pp. 29–43, Jan. 2002.

[49] G. Tochon, J. Chaussot, M. D. Mura, and A. L. Bertozzi, "Object tracking by hierarchical decomposition of hyperspectral video sequences: Application to chemical gas plume tracking," *IEEE Trans. Geosci. Remote Sens.*, vol. 55, no. 8, pp. 4567–4585, Aug. 2017.

[50] A. Mian and R. Hartley, "Hyperspectral video restoration using optical flow and sparse coding," *Opt. Exp.*, vol. 20, no. 10, pp. 10658–10673, 2012.

Yang Xu (S'14–M'16) received the B.Sc. degree in applied mathematics and the Ph.D. degree in pattern recognition and intelligence systems from the Nanjing University of Science and Technology (NUST), Nanjing, China, in 2011 and 2016, respectively.

He is currently a Lecturer with the School of Computer Science and Engineering, NUST. His research interests include hyperspectral image classification, hyperspectral detection, image processing, and machine learning.

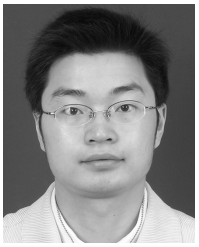

Zebin Wu (M'13–SM'17) was born in Zhejiang, China, in 1981. He received the B.Sc. and Ph.D. degrees in computer science and technology from the Nanjing University of Science and Technology, Nanjing, China, in 2003 and 2007, respectively.

In 2016, he joined the Department of Mathematics, University of California at Los Angeles, Los Angeles, CA, USA, as a Visiting Scholar. He was a Visiting Scholar with the Hyperspectral Computing Laboratory, Department of Technology of Computers and Communications, Escuela Politécnica, University of Extremadura, Cáceres, Spain, from 2014 to 2015. He is currently a Professor with the School of Computer Science and Engineering, Nanjing University of Science and Technology. His research interests include hyperspectral image processing, high-performance computing, and computer simulation.

Jocelyn Chanussot (M'04–SM'04–F'12) received the M.Sc. degree in electrical engineering from the Grenoble Institute of Technology (Grenoble INP), Grenoble, France, in 1995, and the Ph.D. degree from Savoie University, Annecy, France, in 1998.

In 1999, he was with the Geography Imagery Perception Laboratory for the Delegation Generale de l'Armement, French National Defense Department, Arcueil, France. Since 1999, he has been with Grenoble INP, where he was an Assistant Professor from 1999 to 2005 and an Associate Professor from 2005 to 2007, and is currently a Professor of signal and image processing. He was a member of the Institut Universitaire de France, Paris, France, from 2012 to 2017. Since 2013, he has been an Adjunct Professor with the University of Iceland, Reykjavík, Iceland. He is conducting his research with the Grenoble Images Speech Signal and Control Laboratory, Saint-Martin-d'Hères, France. His research interests include image analysis, multicomponent image processing, nonlinear filtering, and data fusion in remote sensing.

Dr. Chanussot was a member of the IEEE Geoscience and Remote Sensing Society Administrative Committee from 2009 to 2010 and in charge of membership development. He was also a member of the Machine Learning for Signal Processing Technical Committee of the IEEE Signal Processing Society from 2006 to 2008. He was the founding President of the IEEE Geoscience and Remote Sensing French Chapter from 2007 to 2010. He was a recipient of the 2010 IEEE Geoscience and Remote Sensing Society Chapter Excellence Award and a co-recipient of the Nordic Signal Processing Symposium 2006 Best Student Paper Award, the IEEE GRSS 2011 Symposium Best Paper Award, the IEEE GRSS 2012 Transactions Prize Paper Award, and the IEEE GRSS 2013 Highest Impact Paper Award. He was the General Chair of the first IEEE GRSS Workshop on Hyperspectral Image and Signal Processing: Evolution in Remote Sensing (WHISPERS). He was the Chair from 2009 to 2011, the Co-Chair of the GRS Data Fusion Technical Committee from 2005 to 2008, and the Program Chair of the IEEE International Workshop on Machine Learning for Signal Processing in 2009. He was an Associate Editor of the IEEE GEOSCIENCE AND REMOTE SENSING LETTERS from 2005 to 2007 and the *Pattern Recognition* from 2006 to 2008. He was the Editor-in-Chief of the IEEE JOURNAL OF SELECTED TOPICS IN APPLIED EARTH OBSERVATIONS AND REMOTE SENSING from 2011 to 2015. Since 2007, he has been an Associate Editor of the IEEE TRANSACTIONS ON GEOSCIENCE AND REMOTE SENSING. He was a Guest Editor of the PROCEEDINGS OF THE IEEE in 2013 and the IEEE SIGNAL PROCESSING MAGAZINE in 2014.

Mauro Dalla Mura (S'08–M'11) received the Laurea (B.E.) and Laurea specialistica (M.E.) degrees in telecommunication engineering from the University of Trento, Trento, Italy, in 2005 and 2007, respectively, and the joint Ph.D. degree in information and communication technologies (telecommunications area) from the University of Trento, and in electrical and computer engineering from the University of Iceland, Reykjavík, Iceland, in 2011.

In 2011 he was a Research Fellow at Fondazione Bruno Kessler, Trento, conducting research on computer vision. He is currently an Assistant Professor with the Grenoble Institute of Technology, Grenoble, France. He is conducting his research at the Grenoble Images Speech Signals and Automatics Laboratory, Saint-Martin-d'Hères, France. His research interests include remote sensing, image processing, pattern recognition, mathematical morphology, classification, and multivariate data analysis.

Dr. Dalla Mura was a recipient of the IEEE GRSS Second Prize in the Student Paper Competition of the 2011 IEEE IGARSS 2011 and a co-recipient of the Best Paper Award of the *International Journal of Image and Data Fusion* during 2012–2013 and the Symposium Paper Award for IEEE IGARSS 2014. He served as a Secretary for the IEEE GRSS French Chapter from 2013 to 2016. He is the President of the IEEE GRSS French Chapter during 2016–2019.

Andrea L. Bertozzi (M'14) received the B.A., M.A., and Ph.D. degrees in mathematics from Princeton University, Princeton, NJ, USA, in 1987, 1988, and 1991, respectively.

She was on the faculty of the University of Chicago, Chicago, IL, USA, from 1991 to 1995, and Duke University, Durham, NC, USA, from 1995 to 2004. From 1995 to 1996, she was the Maria Goeppert-Mayer Distinguished Scholar at the Argonne National Laboratory, Lemont, IL, USA. Since 2003, she has been a Professor of mathematics with the University of California at Los Angeles, Los Angeles, CA, USA, where she is currently the Director of applied mathematics. In 2012, she was appointed the Betsy Wood Knapp Chair of Innovation and Creativity. Her research interests include image inpainting, image segmentation, cooperative control of robotic vehicles, swarming, and fluid interfaces, and crime modeling.

Dr. Bertozzi is a fellow of the Society for Industrial and Applied Mathematics, the American Mathematical Society, and the American Physical Society. She was a recipient of a Sloan Foundation Research Fellowship, the Presidential Career Award for Scientists and Engineers, and the SIAM Kovalevsky Prize in 2009. She has served as a Plenary/Distinguished Lecturer for both SIAM and AMS and is an Associate Editor of the SIAM journals on *Multiscale Modelling and Simulation, Mathematical Analysis, and Image Processing*. She also serves on the Editorial Board of *Interfaces and Free Boundaries, Applied Mathematics Research Express, Nonlinearity, Applied Mathematics Letters, Mathematical Models and Methods in Applied Sciences*, the *Journal of Nonlinear Science*, the *Journal of Statistical Physics, Communications in Mathematical Sciences, Nonlinear Analysis: Real World Applications, and Advances in Differential Equations.*

Zhihui Wei was born in Huaian, China, in 1963. He received the B.Sc. and M.Sc. degrees in applied mathematics and the Ph.D. degree in communication and information system from South East University, Nanjing, China, in 1983, 1986, and 2003, respectively.

He is currently a Professor and a Doctoral Supervisor with the Nanjing University of Science and Technology, Nanjing. His research interests include partial differential equations, mathematical image processing, multiscale analysis, sparse representation, and compressive sensing.